An efficient naphthalene imide-based interface engineering material for enhancing perovskite photovoltaic performance and stability

Helin Wang[†,‡], Yu Guo[§,], Lanlan He[§,*], Lars Kloo[§], Jun Song[†,*], Junle Qu[†], Peng-Cheng Qian[⊥,*], Wai-Yeung Wong[‡,ǁ,*]*

[†] Center for Biomedical Optics and Photonics (CBOP) & College of Physics and Optoelectronic Engineering, Key Laboratory of Optoelectronic Devices and Systems, Shenzhen University, Shenzhen 518060, Guangdong, P. R. China.

[‡] Department of Applied Biology and Chemical Technology, The Hong Kong Polytechnic University, Hung Hom, Kowloon, Hong Kong 999077, P. R. China.

[§] Applied Physical Chemistry, Department of Chemistry, KTH Royal Institute of Technology, SE-10044 Stockholm, Sweden.

[ǁ] The Hong Kong Polytechnic University Shenzhen Research Institute, Shenzhen 518057, Guangdong, P. R. China.

[⊥] Key Laboratory of Environmental Functional Materials Technology and Application of Wenzhou City, Institute of New Materials & Industry Technology, College of Chemistry & Materials Engineering, Wenzhou University, Wenzhou 325035, P. R. China.

[*] Corresponding authors.

E-mail: yg2@kth.se (Y. Guo), lanlanhe@kth.se (L. He), songjun@szu.edu.cn (J. Song), qpc@wzu.edu.cn (P.-C. Qian), wai-yeung.wong@polyu.edu.hk (W.-Y. Wong).

KEYWORDS: interface engineering; naphthalene imide; surface passivation; theoretical calculation; perovskite solar cell.

ABSTRACT: The ways to overcome surface charge recombination and poor interface contact are still the central challenges for the development of inorganic-organic hybrid halide perovskite solar cells (PSCs). PCBM is commonly employed in PSCs, but it has some disadvantages including high charge recombination and poor surface coverage. Therefore, the addition of an interfacial engineering layer showing efficient surface passivation, electron extraction, and excellent interface contact can solve the above problems. Furthermore, by employing interface engineering with a spike structure of the energy levels, the reduced energy losses are beneficial to elevating the open-circuit voltage (V_{oc}) in PSCs. Herein, the linear naphthalene imide dimer containing an indacenodithiophene unit (IDTT2NPI) has been developed as an excellent interface engineering material to strengthen the perovskite performance. The introduction of a spike interface on the top of a methylammonium lead triiodide ($MAPbI_3$) film resulted in a high V_{oc} of 1.12 V with the optimal efficiency reaching 20.2%. The efficiency enhancement can be traced to the efficient surface passivation and enhanced interface contact. The mechanism of IDTT2NPI as the interface engineering layer was investigated by both experiments and theoretical calculations. This work provides a promising naphthalene imide-based interfacial material for high-efficiency and stable PSCs.

INTRODUCTION

Inorganic-organic hybrid perovskite materials are characterized by beneficial photovoltaic properties, for instance, small bandgap, high carrier mobility, long exciton diffusion length, and

solution processability. All these properties have earned widespread interest in the field of semiconductor materials.[1-3] By employing high-efficiency perovskite materials to fabricate thin-film solar cells, device efficiencies above 25% have been demonstrated, which suggests that PSCs have a great potential for future commercialization.[4-6] It is undeniable that the key issue restricting the development of PSCs is still the device efficiency and stability.[7-9] Despite the fact that the PSCs can offer high power conversion efficiencies (*PCE*), surface defects of perovskite materials and poor interface contacts in the devices are important issues that retard the improvement of device performance and stability. On the one hand, there are incompletely coordinated lead atoms on the perovskite surface, which would result in the generation of surface recombination centers.[10-13] Trap-assisted recombination could lead to energy losses in the device, which is manifested by a significant decrease in the V_{oc}. On the other hand, a poor interface contact mainly occurs at the interface between the perovskite film and the carrier transport layer. If the bottom layer (with respect to a deposition order in the manufacturing process) is not flat enough, the perovskite film deposited on top may form pinholes; if the top layer is not smoothly covered, the perovskite film would be in contact with the electrode material. Hence, poor interface contact may cause ion migration in the perovskite layer, and water vapor may as well penetrate into the perovskite film, hence causing degradation of the perovskite material with poor device stability.[14-18] Based on the above discussion, two significant problems may arise at the interface between the layers. Thus, the development of efficient interface engineering materials is key to solving the above problems.

Organic small molecule semiconductor materials as the interface engineering material can be used to passivate surface perovskite traps and elevate the interface contact.[19-21] According to some literature results, heteroatoms or carbonyl groups in the structure of the organic

semiconductor materials form weak coordination bonds or hydrogen bonds to lead atoms at the interface of the perovskite films.[22-26] This type of intermolecular interaction has the potential to reduce the effect of surface defects, thereby inhibiting recombination losses. In addition, the interface engineering material, which is capable of forming a spike structure in the PSCs, may improve the interface carrier transfer path and thus reduce the surface recombination.[27] Therefore, the mitigation of the effect of surface defects may effectively reduce the problem of energy losses in the device, thereby further improving the device performance. Moreover, the addition of the interface engineering layer could improve the coverage of perovskite film and effectively protect the perovskite film, thus suppressing ion migration to enhance the device stability.[28-30] To the best of our knowledge, the p-i-n structure contributes to low-temperature fabrication to allow spin-coating of all device layers in contrast to the more commonly utilized n-i-p device structure. This offers a clear potential in the field of flexible PSCs. PCBM is usually employed as the electron transport material (ETL) for inverted devices. But the higher density of surface recombination centers and poor interface contact are inevitable problems when PCBM is used.[31-33] As a result, the research on suitable interface engineering material to be deposited between the perovskite film and the PCBM layer will be crucial for the development of inverted PSCs. Compared with the existing and commercialized interface materials, the development of novel interface materials with excellent surface passivation and electron extraction performance has lagged behind. Moreover, the naphthalene imide-based semiconductors as the ETL could improve the PSC's performance and stability due to their excellent electron transport property.[34-38] Therefore, we aim to develop efficient naphthalene imide-based interface engineering materials for high-efficiency PSCs with an inverted device structure, which is of great significance to the innovation of the PSC filed.

In this work, IDTT2NPI has been developed by utilizing two classical organic reactions with the advantage of their high yields and low cost of synthesis. Because of its largely planar conjugated framework, IDTT2NPI exhibits excellent solubility in many organic solvents, thermal stability, and high electron-transport property. Hence, IDTT2NPI acts as an interfacial layer to strengthen the device performance. Through using a stepwise modelling approach involving classical molecular dynamics (CMD), static density functional theory (DFT) and ab initio molecular dynamics (AIMD) in combination with experiments, we can show that the carbonyl groups of IDTT2NPI are central for the coordination to lead atoms at the $MAPbI_3$ interface. The IDTT2NPI coordination may passivate the perovskite surface defects together with improving the interface contact. In addition, it is noteworthy to mention that the introduction of a novel spike structure strategy at the $MAPbI_3$ film and the PCBM layer interface efficiently reduces energy losses, which boosts the V_{oc} of the resulting device to 1.12 V resulting in a PCE as high as 20.2%. These results suggest that IDTT2NPI may become a commercially viable and efficient interface engineering material for high-efficiency and stable PSCs based on an inverted device structure.

RESULTS AND DISCUSSION

IDTT2NPI was synthesized by employing amidation and Stille coupling reactions, and the total yield is 69%. As a result, compared with the cost of PCBM (2592 \$ g^{-1}), the cost of IDTT2NPI synthesis was estimated to 240 \$ g^{-1}, implying that it is feasible for the IDTT2NPI to serve as the interface engineering material with commercial potential. The synthetic route and methods used are depicted in Scheme S1 and Supporting Information. The IDTT2NPI structure

was characterized by NMR spectroscopy and HRMS spectrometry, and the results are depicted in Figures S1-S3. The UV-Vis spectra of IDTT2NPI were recorded in dichloromethane and in the form of a thin film as shown in Figure S4. The thermal stability of IDTT2NPI was investigated by thermogravimetric analysis, and the traces are displayed in Figure S5. The weight loss temperature at 375 ºC under a nitrogen atmosphere was 5%. In addition, IDTT2NPI shows excellent solubility in dichloromethane (more than 20 mg mL^{-1}), chloroform (more than 20 mg mL^{-1}), and chlorobenzene (more than 20 mg mL^{-1}), indicating both excellent thermal stability and feasibility for solution-based device fabrication.

Cyclic voltammetry (CV) was conducted to investigate the electrochemical properties of IDTT2NPI, and the results are depicted in Figure S6. IDTT2NPI exhibits two pairs of red/oxi peaks, which are likely to involve the redox chemistry of the naphthalene imide and indacenodithiophene units in the molecule. The onset reduction potential of IDTT2NPI is -1.21 V in dichloromethane solution, and the first reduction peak is utilized to estimate its lowest unoccupied molecular orbital (LUMO) level. As a result, the LUMO level of IDTT2NPI was found to be -3.87 eV, which is close to the energy level of $MAPbI_3$ and PCBM, thereby fulfilling the requirements of an electronic spike device structure with a potential to reduce energy losses and thereby improve the V_{oc}. According to the LUMO level and the bandgap energy E_g (2.01 eV, as derived from the UV-Vis absorption results), the highest occupied molecular orbital (HOMO) level of IDTT2NPI was found to be -5.88 eV.

Furthermore, the ground-state geometries were used as a tool to explore the energy levels and electron density distribution. As expected, the LUMO electron density is found at the naphthalene imide framework, and the HOMO electron density is primarily found at indacenodithiophene core, as illustrated in Figure S7. The estimated LUMO and HOMO energy

levels are respectively found to be -2.59 and -5.15 eV. These results are in excellent connection with the CV investigation. The current density-voltage (*J-V*) traces of electron-only devices with an architecture of ITO/ZnO/electron transport material/Ca/Al were recorded to reveal the electron mobilities of PCBM and IDTT2NPI by employing the SCLC method as depicted in Figure S8.[39-42] The electron mobilities were found to be 1.14×10^{-3} and 1.23×10^{-3} cm^2 V^{-1} s^{-1} for IDTT2NPI and PCBM, respectively, implying that IDTT2NPI may also be employed as a potential ETL by itself. Overall, IDTT2NPI shows excellent physical properties as the interface engineering material with the potential to improve the device performance.

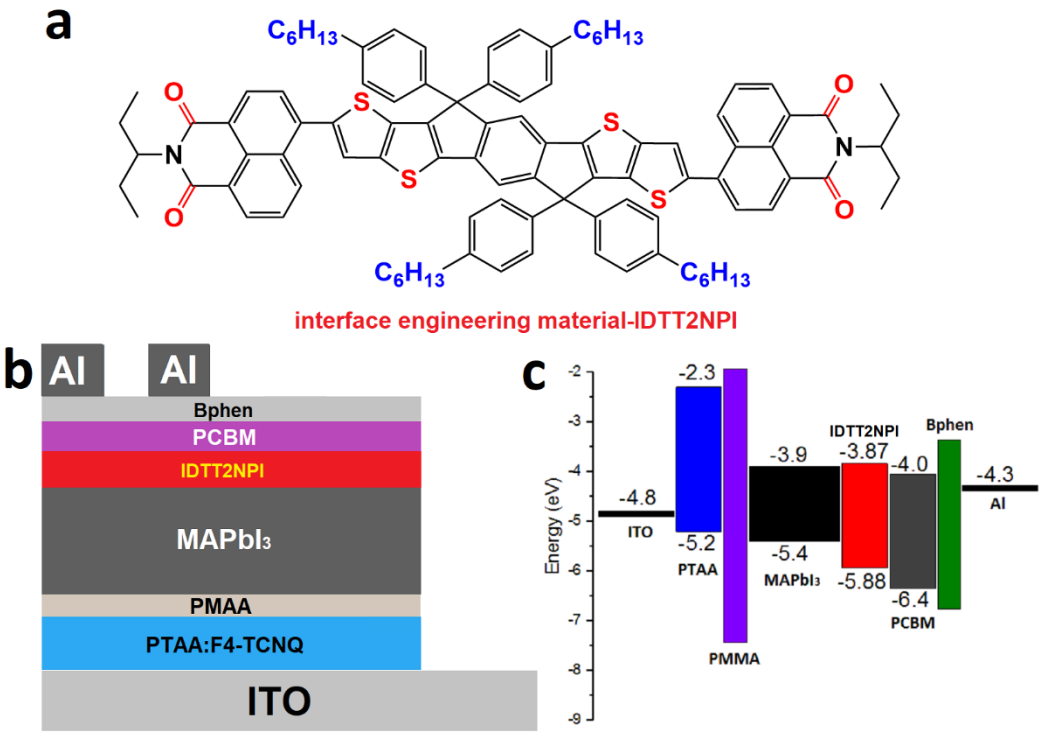

Figure 1. (a) Molecular structure of IDTT2NPI; (b) the inverted PSCs structure in this work; (c) energy levels of materials.

PSCs were manufactured with and without the IDTT2NPI interface layer to understand the influence of the interface engineering layer positioned in between the perovskite film and the

PCBM layer. A device structure was depicted in Figure 1b. F4-TCNQ as a p-type dopant in the hole transport layer was used to enhance the conductivity of the PTAA film due to the exceptional strong electron-accepting ability of F4-TCNQ (its LUMO level is -5.24 eV). The energy level alignment in the inverted PSCs is depicted in Figure 1c. The devices not containing the IDTT2NPI layer were included in this study as the control devices. Due to the difference in the LUMO energy levels for the three materials ($MAPbI_3$, IDTT2NPI, and PCBM) used in this study, a spike energy level structure can be achieved to improve the device performance. Initially, the effect of different film thicknesses of the interfacial layer on the device efficiency was investigated, as shown in Figure S9, and the results are summarized in Table S1. The best-performing device exhibited a PCE of 20.2% when an about 15 nm interfacial layer was employed. The optimal device performance can partly be traced to the excellent film morphology, better than for layers with other thicknesses.

Subsequently, the influence of the interfacial layer on the hysteresis effects in the PSC devices was investigated. *J-V* characteristics were investigated for control devices and for about 15 nm interfacial layer-modified devices. The results in Figure 2a show that a negligible hysteresis occurred in the IDTT2NPI-based devices in contrast to the control devices. According to the equation (1),[43] the hysteresis index (HI) values were respectively found to be 0.025 and 0.00064 for the control and IDTT2NPI-based devices, which indicates that the IDTT2NPI layer indeed reduces the hysteresis in inverted PSCs. As a result, the optimal IDTT2NPI-based device under a forward scan exhibited an improved *PCE* of 20.2%, as compared to 18.3% of the optimal control device, suggesting that the spike structure-based interface engineering applied through IDTT2NPI can improve the device performance. The results are summarized in Table 1.

$$\mathbf{HI} = \frac{J_R(0.8\,V_{oc}) - J_F(0.8\,V_{oc})}{J_R(0.8\,V_{oc})} \quad (1)$$

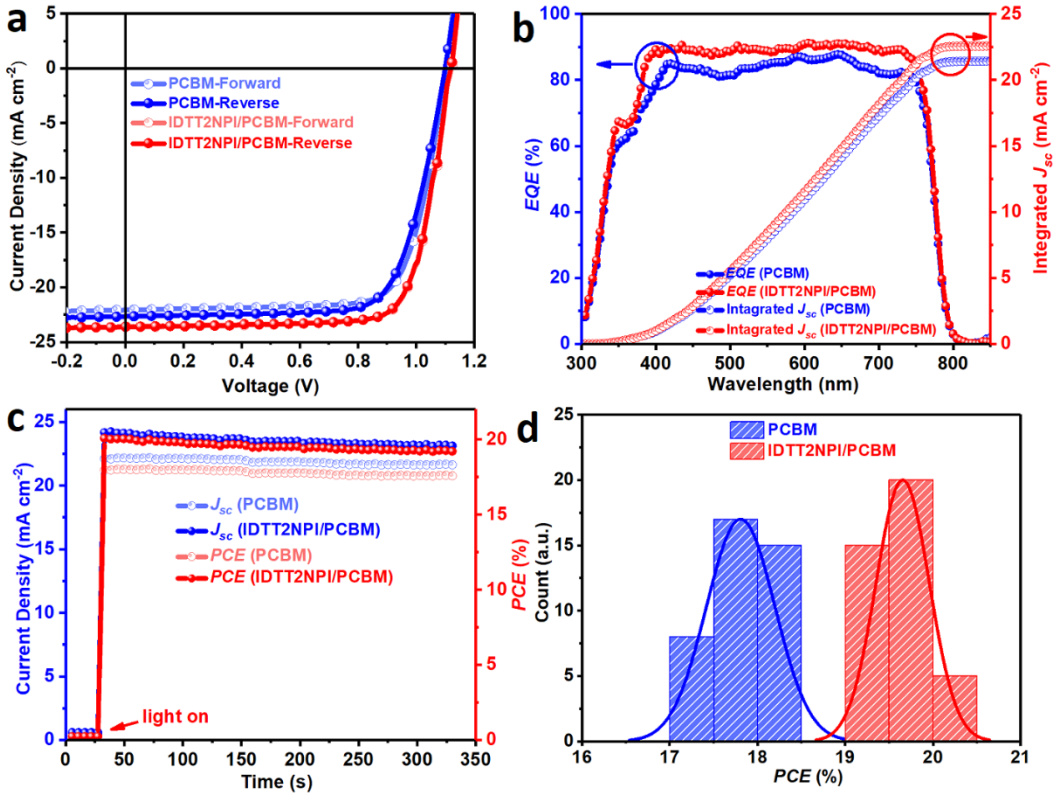

Figure 2. (a) *J-V* curves obtained using forward and reverse scan directions for PSCs without or with IDTT2NPI layer; (b) EQE spectrum and the integrated J_{sc} curves for PSCs with and without IDTT2NPI layer; (c) stabilized photocurrent density and power output at the maximum power point for devices with and without IDTT2NPI layer; (d) statistics of the PCE distribution of PCBM- and IDTT2NPI/PCBM-based devices obtained from forward scan direction (40 devices of each type).

Figure 2b shows the external quantum efficiency (*EQE*) spectra for the control and IDTT2NPI-based devices, and there was a more efficient photoresponse of the IDTT2NPI-modified solar cells. The integral J_{sc} values were estimated to be 21.4 and 22.6 mA cm^{-2} for the control and IDTT2NPI-based devices, respectively, which are in excellent agreement with the

photocurrents obtained from the *J-V* investigation. The IDTT2NPI-based PSCs generated higher photoresponse spectra than the control devices, which revealed the higher J_{sc}. Moreover, the optimal control and IDTT2NPI-based devices respectively exhibited stable photocurrent densities of 21.6 and 23.1 mA cm^{-2}, and stabilized PCEs of 17.6% and 19.2% as depicted in Figure 2c. This emphasizes that the inclusion of an IDTT2NPI interface layer can consistently improve the photocurrent density and PCE. The PCE statistical distribution histograms resulting from the two types of devices are summarized in Figure 2d. The IDTT2NPI-based devices show a much higher average PCE value, (19.7±0.3)% compared with the control devices (17.8±0.4)%. These results agree well with the *J-V* characterization. These results indicate that IDTT2NPI acts as an efficient interfacial layer to achieve high-efficiency PSCs with an inverted device structure.

Table 1. Best performance for the control and IDTT2NPI-based devices.

Conditions	Scan direction	J_{sc} [mA cm^{-2}]	V_{oc} [V]	*FF* [%]	*PCE* [%]
control	FS	22.1	1.10	75.3	18.3
control	RS	22.7	1.10	73.2	18.2
IDTT2NPI	FS	23.5	1.12	76.3	20.2
IDTT2NPI	RS	23.6	1.12	76.2	20.2

In order to get insights into the observed enhancement of the IDTT2NPI-based PSCs, the perovskite film morphology was investigated by scanning electron microscopy (SEM) and atomic force microscopy (AFM). Figures 3a-c show that all three films displayed smooth and pinhole-free film morphologies, and the top-view SEM images of PCEM- or IDTT2NPI/PCBM-coated films exhibit better film coverage than the bare perovskite film. The root-mean-square

(RMS) roughness was estimated to be 18 nm, 14 nm, and 11 nm for the bare perovskite, PCBM- or PCBM/IDTT2NPI-coated films, respectively, and the depth of grain boundaries is also lower as depicted in Figure S10. These results imply that IDTT2NPI can improve the interface contact and generate excellent surface and grain boundary conditions, thereby inhibiting water-induced degradation of the perovskite film. In order to gain insight into the function of the IDTT2NPI layer as an efficient passivator for the perovskite film, also X-ray photoelectron spectroscopy (XPS) was measured to understand the interaction between the layers. The lead and iodine peaks of IDTT2DN-based films shift to the lower binding energies as depicted in Figures S11-S12, indicating the existence of intermolecular interaction. Furthermore, the lead and iodine peak positions do not change significantly after washing with chlorobenzene indicating a strong IDTT2NPI-$MAPbI_3$ interaction. These results demonstrate that IDTT2NPI could passivate the surface traps and thereby strengthen the interface contacts.

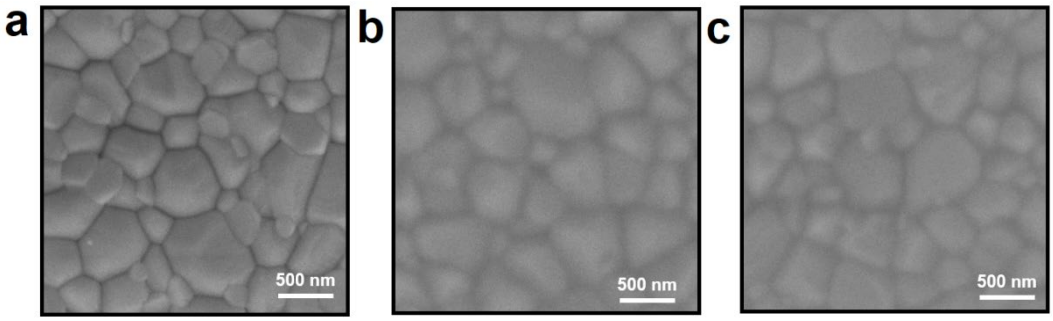

Figure 3. Top-view SEM images of the $MAPbI_3$ film (a), and PCBM (b)-, or IDTT2NPI/PCBM (c) -modified $MAPbI_3$ films.

For a deeper insight into the interaction between the IDTT2NPI and $MAPbI_3$ layers, steady-state photoluminescence (PL) spectra of $MAPbI_3$ films with various modifications were conducted. PL quenching was clearly observed when an ETL has been applied in Figure 4a. As

expected, the IDTT2NPI/PCBM-based film shows a more pronounced quenching than the other materials, suggesting that the IDTT2NPI layer could improve the electron extraction efficiency from the perovskite film to the PCBM layer. The thickness of the IDTT2NPI interfacial layer is very thin (about 15 nm), so the addition of IDTT2NPI has little effect on the electron transport in the device. Moreover, the focus is that the IDTT2NPI layer can passivate the surface defects and improve the interface contact, which is more conducive to electron extraction and transport. It is noteworthy to mention that the PL intensity of the IDTT2NPI/PCBM-modified film does not change after washing with chlorobenzene, which agrees well with the above mentioned XPS results. In order to further investigate the IDTT2NPI passivation effect, the V_{oc} versus light intensity (I) curve was recorded. The V_{oc} and I are related according to equation (2),[44] where k, T, and q represent the Boltzmann constant, the temperature in Kelvin, and the charge, respectively. This equation indicates that the slope of V_{oc} vs. I is associated with the trap-assisted recombination, as depicted in Figure 4b. A linear model fitted to the data rendered a slope from the PCBM-based devices (1.42 kT q^{-1}) and the IDTT2NPI/PCBM-based devices (1.30 kT q^{-1}) implying that the spike structure-based interface engineering suppresses the trap-assisted recombination and consequently reduces the energy losses, which in turn contributes to the improvement of the V_{oc} and the *PCE*.

$$\boldsymbol{\delta V_{oc} = \left(\frac{kT}{q}\right) \ln(I) + \text{const}} \qquad (2)$$

In order to gain a deeper understanding of the film passivation on the device performance, electron-only SCLC devices were measured to extract information on trap densities and electron mobilities in the two types of devices. The structure of ITO/SnO_2/$MAPbI_3$/IDTT2NPI/ PCBM/Al was fabricated, and a device without an IDTT2NPI layer was used as the control. Evaluation of

the data in Figure 4c[45] renders a lower trap density of 1.65×10^{15} cm^{-3} for the IDTT2NPI-based devices as compared with the control devices (2.35×10^{15} cm^{-3}). The results are summarized in Table S2, and the results show that the surface defects of the perovskite films are reduced upon the addition of the IDTT2NPI layer. In addition, higher electron mobility of 0.028 cm^2 V^{-1} s^{-1} was obtained for the devices based on the IDTT2NPI material as compared to that of the control device (0.018 cm^2 V^{-1} s^{-1}). These results directly confirm that spike structure-based interface engineering plays a significant role to strengthen defect passivation and electron transport for the PSCs. In order to demonstrate the effect of the IDTT2NPI layer on the performance improvement, time-resolved photoluminescence (TRPL) spectra of a bare perovskite film and two modified films were conducted, and the TRPL decays were modelled using a biexponential decay function. Figure 4d displays that the obtained decay lifetimes for the two types of devices and the fluorescence lifetime microscopy images are shown in Figure S13. Both more efficient PL quenching and faster TRPL decays were observed upon the incorporation of the IDTT2NPI layer, which presents a signature of an improved interface electron transfer. Moreover, the decay lifetimes of the IDTT2NPI-modified film are slightly shorter than for the control film, which indicates that interface engineering renders a higher electron injection rate.

Theoretical calculations. In order to describe the interaction between $MAPbI_3$ and the IDTT2NPI molecule, we performed theoretical calculations in three steps. Firstly, classical molecular dynamics (CMD) simulation was employed by using OPLSAA force field to study the interaction between $MAPbI_3$ and IDTT2NPI and generate a rough coordination pattern of the perovskite-IDTT2NPI interaction based on one IDTT2NPI molecule and a comparably big perovskite slab, in which the methylamine cations were substituted for Cs^+ cations to avoid orientational effects. Secondly, the geometry optimization of a static density functional theory

(DFT) was performed to further identify the predominant interaction sites between $CsPbI_3$ and the IDTT2NPI molecule. Finally, ab initio molecular dynamics (AIMD) simulation was used to accurately investigate the dynamic structural flexibility of the IDTT2NPI-$CsPbI_3$ interaction.

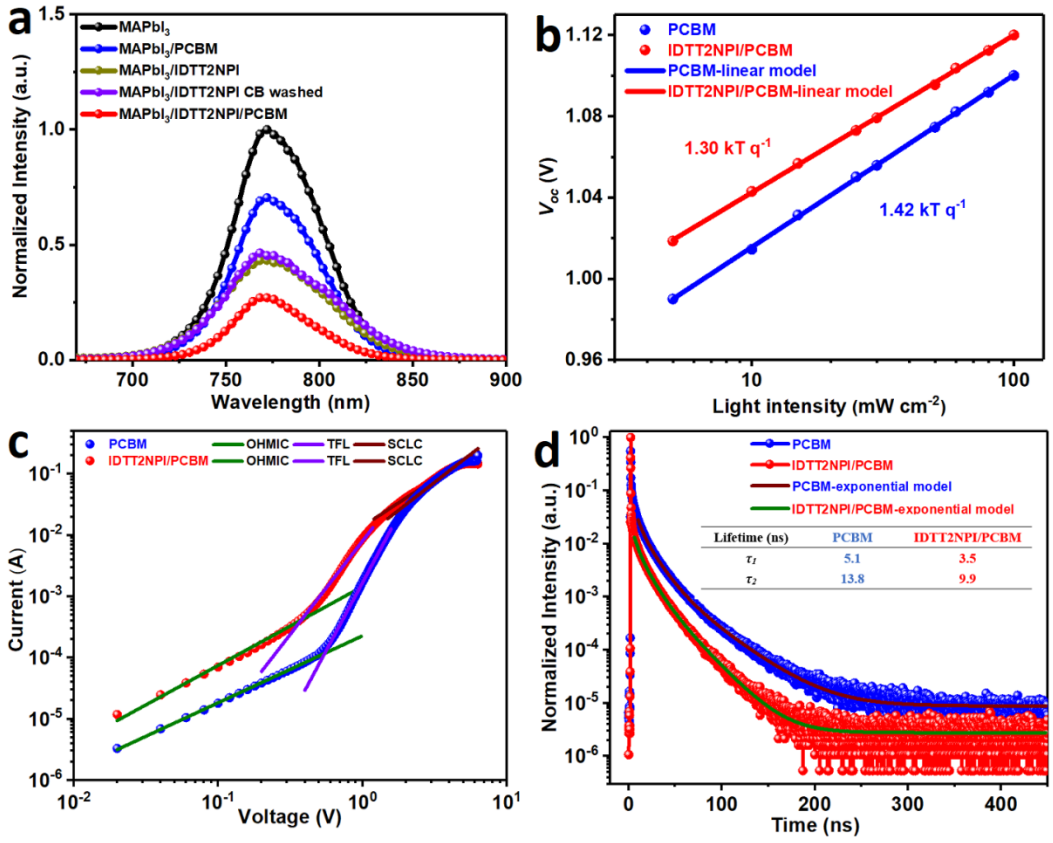

Figure 4. (a) Steady-state photoluminescence spectra for $MAPbI_3$ films, naked and coated by PCBM or IDTT2NPI/PCBM; (b) V_{oc} versus light intensity for PCBM- and IDTT2NPI/PCBM-based devices (symbols), together with a linear model fitted to the data (solid lines); (c) current-voltage traces of PCBM- and IDTT2NPI/PCBM-based $MAPbI_3$ films investigated by the SCLC method; (d) TRPL spectra for naked $MAPbI_3$ films and those coated by PCBM or IDTT2NPI/PCBM.

Classical molecular dynamics simulation. In order to explore the interaction between the model perovskite $CsPbI_3$ slab and an IDTT2NPI molecule, a 5 ns CMD simulation was performed. The initial and equilibrium structures are displayed in Figures S14 and S15, respectively. The equilibrium structure shows that the strong interaction between $CsPbI_3$ and the IDTT2NPI molecule most likely can be attributed to the interaction between O, rather than S, atoms in the IDTT2NPI molecule with Pb atoms at the perovskite surface. The radial distribution function (RDF) between Pb and O atoms $g_{PbO(r)}$, as well as between Pb and S atoms $g_{PbS(r)}$, were investigated and are shown in Figure S16. From $g_{PbO(r)}$, we can note that the first peak of $g_{PbO(r)}$ ranges from 2.75-3.65 Å and the maximum value is located at 3.00 Å. This result suggests that the nearest distance between O (in IDTT2NPI) and Pb (in $CsPbI_3$) is 2.75 Å and the distance of the highest probability is 3.00 Å. This suggests the binding distance at the level of CMD. On the other side, in the RDF of $g_{PbS(r)}$, the first peak of $g_{PbS(r)}$ ranges from 4.45-6.19 Å and the maximum value is located at 5.47 Å. Compared with the distances recorded for the Pb-O contacts, as well as compared to typical Pb-O and Pb-S distances, this suggests that partly due to the greater planar rigidity and the steric hindrance of the side chains, the Pb-S interaction is much weaker and that the predominant interaction between IDTT2NPI and the perovskite surface is mediated by the Pb-O interactions.[46]

Static density functional theory. The structure obtained from static DFT optimization performed with the preferred coordination inferred by the CMD simulations is similar to that obtained from CMD simulation, as shown in Figure 5. The IDTT2NPI coordinates to the surface of the perovskite slab after rotating two of its alkyl chains. Compared with the results of CMD, the bonding interaction between IDTT2NPI and the perovskite model shows that one carbonyl

oxygen of the side chain is strongly bonded to Pb at a distance of 2.71 Å, and another carbonyl oxygen on the opposite side chain is weakly bonded to Pb with a bond distance of 3.09 Å.

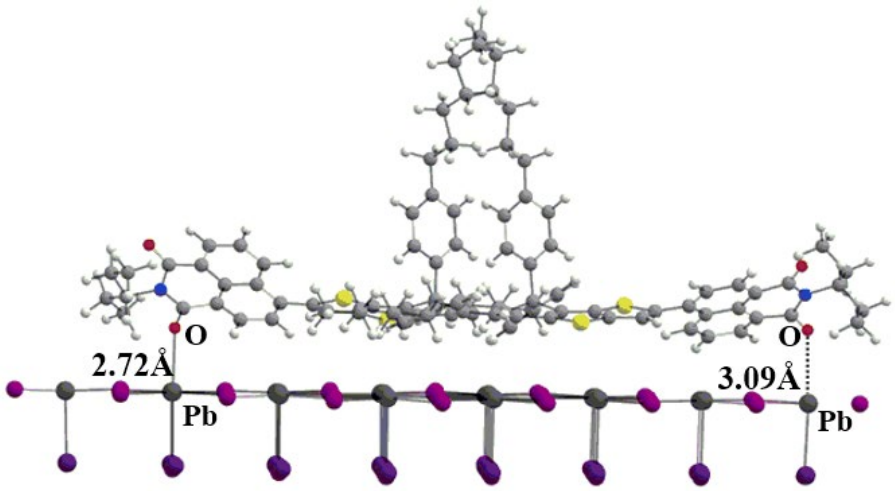

Figure 5. The DFT optimized structure of the IDTT2NPI-$CsPbI_3$ model system.

Ab-initio molecular dynamics simulation. In order to further investigate the interaction between IDTT2NPI and the perovskite surface, we employed AIMD to simulate the model system of $CsPbI_3$ and the IDTT2NPI molecule. The dynamics of the key atomic distances of Pb-O and Pb-S are outlined in Figure 6a, which are displayed by red and blue curves, respectively. It can be noted that both Pb-O and Pb-S distances are quite stationary. The Pb-O distances range from 2.32-3.55 Å, and the Pb-S distances range from 3.92-5.17 Å, respectively. This again suggests the preference of Pb-O interaction over Pb-S interaction. Figure 6b shows the dynamics of the distances of Pb-S (blue, just as in Fig. 6a) and I-S (yellow), which range from 3.92-5.17 Å and 3.72-4.50 Å, respectively. This suggests that the Pb-S interaction may be weaker than the I-S interaction, which can be explained by a charge distribution analysis. Table S3 lists the average charge distributions of Mulliken population analysis of each step AIMD simulation on O, N, S, Pb and I atoms. The charge distribution of O, N, S, Pb and I are -0.53, -0.55, 0.21, 0.80, and -

0.53 e, respectively. This indicates that there is an electrostatic attraction between Pb and O, whereas an electrostatic repulsion between Pb and S. This may contribute to the closer Pb-O interaction. Although the negative charge of N would suggest a potential for strong electrostatic interaction, steric hindrance blocks its interaction with the surface. The S atoms may be closer to I than to Pb because of the electrostatic interaction, which is, however, still longer than the Pb-O contacts. Overall, the strongest interaction between IDTT2NPI and the perovskite model $CsPbI_3$ can be linked to the close Pb-O contacts. Above all, these results clearly demonstrate that the carbonyl groups of IDTT2NPI can coordinate to Pb atoms on the perovskite surface, which is beneficial for efficient surface passivation and improved interface contact.

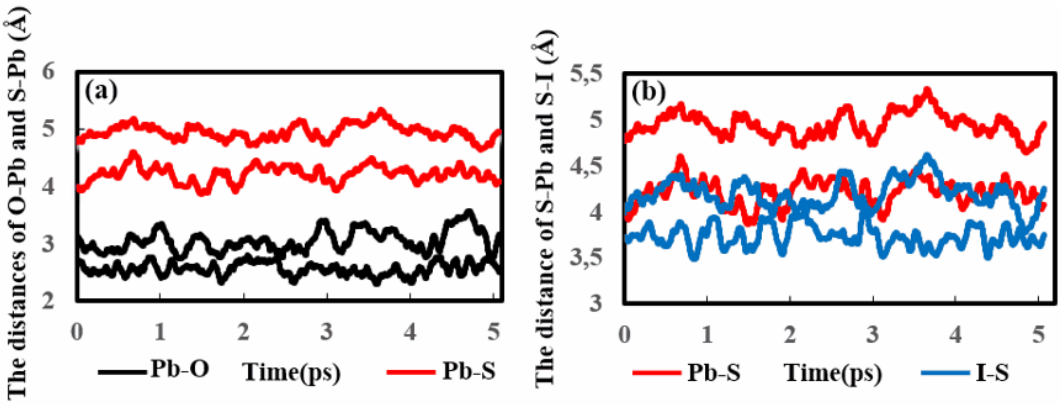

Figure 6. (a) The distances of Pb-O and Pb-S for the IDTT2NPI-$CsPbI_3$ model system during AIMD simulation; (b) the distances of I-S and Pb-S for IDTT2NPI-$CsPbI_3$ model system during AIMD simulation.

Finally, the stability of the devices was carried out. Figure S17 displays the stability of the two types of devices encapsulated under the ambient atmosphere at about 25% humidity. After storage for 150 h, the device efficiency of the control devices degrades by 40% of the initial value, whereas that of the IDTT2NPI-based devices maintained 60% of the initial performance

under the same conditions. These results may be attributed to the surface passivation retarding the degradation of the perovskite film.[47, 48] Also water contact angles were determined, as depicted in Figure S18. The IDTT2NPI-coated film shows a slightly larger contact angle, although both films are highly hydrophobic. This indicates that the main effect of IDTT2NPI lies in the smooth films formed with few pin-holes, cracks, and similar defects.

CONCLUSION

In summary, a linear conjugated NDI dimer (IDTT2NPI) has been developed and combines the advantages of facile synthesis, low cost, and potential for commercialization. IDTT2NPI exhibits excellent solubility, thermal stability, suitable energy levels, and high electron mobility qualifying it as a promising interface engineering material for inverted PSCs with the aim to improve device performance and stability. The best *PCE* of IDTT2NPI-based device amounted to 20.2%, to be compared to that of a PCBM-only control device (18.3%). Most likely this can be attributed to efficient electron extraction, surface passivation, and interface contact mediated by IDTT2NPI. In addition, spike structure-based interface engineering is suggested to suppress trap-assisted recombination losses between the perovskite film and the PCBM layer resulting in an improvement of V_{oc} and *PCE*. Furthermore, by using classical molecular dynamics, density functional theory, ab initio molecular dynamics, XPS, and steady-state PL, the intermolecular interaction between the perovskite film and the IDTT2NPI layer can be elucidated. As a result, the carbonyl groups in IDTT2NPI coordinate to lead atoms at the surface of perovskite films. These results identify important guidelines in the search for organic small molecules to passivate the surface defects of the perovskite film.

EXPERIMENTAL SECTION

Calculation methods. In order to describe the interaction between the $MAPbI_3$ and the IDTT2NPI molecule more accurately, three methods including classical molecular dynamics (CMD) simulation, static density functional theory (DFT) and ab initio molecular dynamic (AIMD) were utilized. The atoms of the perovskite model slab were kept fixed in all calculations. Firstly, classical molecular dynamics (CMD) simulations were performed by using the Tinker 8.7 package employing the OPLS-AA force field at a temperature of 298 K. The Packmol software was used to build the initial model system for CMD consisting of 741 atoms including the perovskite slab and the IDTT2NPI molecule. In order to avoid less important orientational and symmetrical effects, the methyl ammonium cations were replaced by Cs^+ cations in the perovskite model ($CsPbI_3$). NVT (particle number, volume, and temperature) ensemble and three-dimensional periodic boundary conditions were employed with the box edge lengths of 44.0, 32.4, and 42.0 Å. The total time of CMD simulation was 5 ns and the time step was set to 1 fs. The cut-off radius was set to 16.2 Å, which was half of the minimum box length for non-bonded interactions. Berendsen thermostats were adopted to keep the temperature constant during the simulation. Secondly, DFT geometry optimization of the complex of $CsPbI_3$ and IDTT2NPI was performed using Gaussian16 to investigate the nature of interaction between the IDTT2NPI molecule and the perovskite slab $CsPbI_3$. The model consists of a two-layer $CsPbI_3$ model and one IDTT2NPI molecule (316 atoms in total). The slab-molecule interface consists of Pb and I. Basis sets based on SDD effective core potentials (ECPs) were used for $CsPbI_3$ and 6-311G** for the IDTT2NPI molecule. Thirdly, in order to study the dynamic processes of flexibility of the perosvlite-molecule interaction, ab initio molecular dynamics (AIMD)

simulations were performed by the TeraChem 1.9.3 code with a canonical ensemble thermostat (NVT). The calculations were performed using the functional B3LYP and basis sets of 6-31G* quality. LANL2DZ effective core potentials were used for $CsPbI_3$. Using the DFT optimized structure as the starting point, Born-Oppenheimer MD was run for 5 ps at 298 K, using a step size of 1 fs.

ASSOCIATED CONTENT

Supporting Information

The Supporting Information is available free of charge on the ACS Publications website at DOI.

Materials and characterization, device fabrication and characterization, synthesis of IDTT2NPI, calculation methods, and supporting tables and figures.

AUTHOR INFORMATION

Corresponding Author

*Y. Guo. E-mail: yg2@kth.se.

*L. He. E-mail: lanlanhe@kth.se.

*J. Song. E-mail: songjun@szu.edu.cn.

*P.-C. Qian. E-mail: qpc@wzu.edu.cn.

*W.-Y. Wong. E-mail: wai-yeung.wong@polyu.edu.hk.

Notes

The authors declare no competing financial interest.

ACKNOWLEDGMENTS

All authors would like to acknowledge the NKRDPC (2018YFC0910602). J. S. would like to gratefully acknowledge the KPDEGP (2016KCXTD007). W.-Y. W. would like to acknowledge supports from the STICSM (JCYJ20180507183413211); the NFSC (51873176); the HKRGC (PolyU 123384/16P, C5037-18G); the HKPU (1-ZE1C, 847S) for the financial support. J. Q. would like to gratefully thank the NSFC (61775145, 61525503, 61620106016, 61835009). The Swedish Research Council and Stiftelsen Olle Eriksson Byggmästare are also acknowledged for their support. P.-C. Q. thanks to the Foundation of Wenzhou Science & Technology Bureau (No. W20170003) and the NFSC (No. 21828102) for the support.

REFERENCES

[1] Yang, W. S.; Park, B.-W.; Jung, E. H.; Jeon, N. J.; Kim, Y. C.; Lee, D. U.; Shin, S. S.; Seo, J.; Kim, E. K.; Noh, J. H.; Seok, S. Iodide Management in Formamidinium-Lead-Halide-Based Perovskite Layers for Efficient Solar Cells. *Science* **2017**, *356*, 1376-1379. DOI 10.1126/science.aan2301.

[2] Yang, W. S.; Noh, J. H.; Jeon, N. J.; Kim, Y. C.; Ryu, S.; Seo, J.; Seok, S. High-Performance Photovoltaic Perovskite Layers Fabricated through Intramolecular Exchange. *Science* **2015**, *348* 1234-1237. DOI 10.1126/science.aaa9272.

[3] Fu, Q.; Tang, X.; Huang, B.; Hu, T.; Tan, L.; Chen, L.; Chen, Y. Recent Progress on the Long-Term Stability of Perovskite Solar Cells. *Adv. Sci.* **2018**, *5*, No. 1700387. DOI 10.1002/advs.201700387.

[4] Liu, M.; Johnston, M. B.; Snaith, H. J. Efficient Planar Heterojunction Perovskite Solar Cells by Vapour Deposition. *Nature* **2013**, *501*, 395-398. DOI 10.1038/nature12509.

[5] Zhou, H.; Chen, Q.; Li, G.; Luo, S.; Song, T.-b.; Duan, H.-S.; Hong, Z.; You, J.; Liu, Y.; Yang, Y. Interface Engineering of Highly Efficient Perovskite Solar Cells. *Science* **2014**, *345*, 542-546. DOI 10.1126/science.1254050.

[6] Min, H.; Kim, M.; Lee, S.; Kim, H.; Kim, G.; Choi, K.; Lee, J. H.; Seok, S. Efficient, Stable Solar Cells by Using Inherent Bandgap of α-Phase Formamidinium Lead Iodide. *Science* **2019**, *366*, 749-753. DOI 10.1126/science.aay7044.

[7] Park, N.-G.; Grätzel, M.; Miyasaka, T.; Zhu, K.; Emery, K. Towards Stable and Commercially Available Perovskite Solar Cells. *Nat. Energy* **2016**, *1*, No. 16152. DOI 10.1038/nenergy.2016.152.

[8] Ahn, N.; Son, D.-Y.; Jang, I.-H.; Kang, S. M.; Choi, M.; Park, N.-G. Highly Reproducible Perovskite Solar Cells with Average Efficiency of 18.3% and Best Efficiency of 19.7% Fabricated via Lewis Base Adduct of Lead (II) Iodide. *J. Am. Chem. Soc.* **2015**, *137*, 8696-8699. DOI 10.1021/jacs.5b04930.

[9] Guo, F.; Qiu, S.; Hu, J.; Wang, H.; Cai, B.; Li, J.; Yuan, X.; Liu, X.; Forberich, K.; Brabec, C. J.; Mai, Y. H. A Generalized Crystallization Protocol for Scalable Deposition of High-Quality Perovskite Thin Films for Photovoltaic Applications. *Adv. Sci.* **2019**, *6*, No. 1901067. DOI 10.1002/advs.201901067.

[10] Zhang, F.; Huang, Q.; Song, J.; Zhang, Y.; Ding, C.; Liu, F.; Liu, D.; Li, X.; Yasuda, H.; Yoshida, K.; Qu, J.; Hayase, S.; Toyoda, T.; Minemoto, T.; Shen, Q. Growth of Amorphous Passivation Layer Using Phenethylammonium Iodide for High-Performance Inverted Perovskite Solar Cells. *Sol. RRL* **2020**, *4*, No. 1900243. DOI 10.1002/solr.201900243.

[11] Zhang, F.; Huang, Q.; Song, J.; Hayase, S.; Qu, J.; Shen, Q. A New Strategy for Increasing the Efficiency of Inverted Perovskite Solar Cells to More Than 21%: High-Humidity Induced Self-Passivation of Perovskite Films. *Sol. RRL* **2020**, *4*, No. 2000149. DOI 10.1002/solr.202000149.

[12] Zhang, F.; Song, J.; Hu, R.; Xiang, Y.; He, J.; Hao, Y.; Lian, J.; Zhang, B.; Zeng, P.; Qu, J.; Interfacial Passivation of the P-Doped Hole-Transporting Layer Using General Insulating Polymers for High-Performance Inverted Perovskite Solar Cells. *Small* **2018**, *14*, No. 1704007. DOI 10.1002/smll.201704007.

[13] Wang, H.; Zhang, F.; Li, Z.; Zhang, J.; Lian, J.; Song, J.; Qu, J.; Wong, W.-Y. Naphthalene Imide Dimer as Interface Engineering Material: An Efficient Strategy for Achieving High-Performance Perovskite Solar Cells. *Chem. Eng. J.* **2020**, *395*, No. 125062. DOI 10.1016/j.cej.2020.125062.

[14] You, J.; Hong, Z.; Yang, Y.; Chen, Q.; Cai, M.; Song, T. B.; Chen, C. C.; Lu, S.; Liu, Y.; Zhou, H.; Yang, Y. Low-Temperature Solution-Processed Perovskite Solar Cells with High Efficiency and Flexibility. *ACS Nano* **2014**, *8*, 1674-1680. DOI 10.1021/nn406020d.

[15] Heo, J. H.; Han, H. J.; Kim, D.; Ahn, T. K.; Lm, S. H.; Hysteresis-Less Inverted $CH_3NH_3PbI_3$ Planar Perovskite Hybrid Solar Cells with 18.1% Power Conversion Efficiency. *Energy Environ. Sci.* **2015**, *8*, 1602-1608. DOI 10.1039/c5ee00120j.

[16] Seo, J.; Park, S.; Kim, Y. C.; Jeon, N. J.; Noh, J. H.; Yoon, S. C.; Seok, S. Benefits of Very Thin PCBM and LiF Layers for Solution-Processed p-i-n Perovskite Solar Cells. *Energy Environ. Sci.* **2014**, *7*, 2642-2646. DOI 10.1039/C4EE01216J.

[17] Jung, H. S.; Park, N. G. Perovskite Solar Cells: from Materials to Devices. *Small* **2015**, *11*, 10-25. DOI 10.1002/smll.201402767.

[18] Zheng, X.; Chen, B.; Dai, J.; Fang, Y.; Bai, Y.; Lin, Y.; Wei, H.; Zeng, X. C.; Huang, J. Defect Passivation in Hybrid Perovskite Solar Cells Using Quaternary Ammonium Halide Anions and Cations. *Nat. Energy* **2017**, *2*, No. 17102. DOI 10.1038/nenergy.2017.102.

[19] Kim, S. S.; Bae, S.; Jo, W. H. A Perylene Diimide-Based Non-Fullerene Acceptor as an Electron Transporting Material for Inverted Perovskite Solar Cells. *RSC Adv.* **2016**, *6*, 19923-19927. DOI 10.1039/c5ra27620a.

[20] Luo, D.; Yang, W.; Wang, Z.; Sadhanala, A.; Hu, Q.; Su, R.; Shivanna, R.; Trindade, G. F.; Watts, J. F.; Xu, Z. Enhanced Photovoltage for Inverted Planar Heterojunction Perovskite Solar Cells. *Science* **2018**, *360*, 1442-1446. DOI 10.1126/science.aap9282.

[21] Liu, K.; Chen, S.; Wu, J.; Zhang, H.; Qin, M.; Lu, X.; Tu, Y.; Meng, Q.; Zhan, X. Fullerene Derivative Anchored SnO_2 for High-Performance Perovskite Solar Cells. *Energy Environ. Sci.* **2018**, *12*, 3463-3471. DOI 10.1039/c8ee02172d.

[22] Noel, N. K.; Abate, A.; Stranks, S. D.; Parrott, E. S.; Burlakov, V. M.; Goriely, A.; Snaith, H. J. Enhanced Photoluminescence and Solar Cell Performance via Lewis Base Passivation of Organic-Inorganic Lead Halide Perovskites. *ACS Nano* **2014**, *8*, 9815-9821. DOI 10.1021/nn5036476.

[23] Sun, C.; Wu, Z.; Yip, H. L.; Zhang, H.; Jiang, X. F.; Xue, Q.; Hu, Z.; Hu, Z.; Shen, Y.; Wang, M.; Huang, F.; Cao, Y. Amino-Functionalized Conjugated Polymer as an Efficient Electron Transport Layer for High-Performance Planar-Heterojunction Perovskite Solar Cells. *Adv. Energy Mater.* **2016**, *6*, No. 1501534. DOI 10.1002/aenm.201501534.

[24] Li, X.; Chen, C.-C.; Cai, M.; Hua, X.; Xie, F.; Liu, X.; Hua, J.; Long, Y.-T.; Tian, H.; Han, L. Efficient Passivation of Hybrid Perovskite Solar Cells Using Organic Dyes with COOH Functional Group. *Adv. Energy Mater.* **2018**, *8*, No. 1800715. DOI 10.1002/aenm.201800715.

[25] Li, N.; Tao, S.; Chen, Y.; Niu, X.; Onwudinanti, C. K.; Hu, C.; Qiu, Z.; Xu, Z.; Zheng, G.; Wang, L. Cation and Anion Immobilization through Chemical Bonding Enhancement with Fluorides for Stable Halide Perovskite Solar Cells. *Nat. Energy* **2019**, *4*, 408-415. DOI 10.1038/s41560-019-0382-6.

[26] Jiang, Q.; Zhao, Y.; Zhang, X.; Yang, X.; Chen, Y.; Chu, Z.; Ye, Q.; Li, X.; Yin, Z.; You, J. Surface Passivation of Perovskite Film for Efficient Solar Cells. *Nat. Photonics* **2019**, *13*, 460-466. DOI 10.1038/s41566-019-0398-2.

[27] Kapil, G.; Ripolles, T. S.; Hamada, K.; Ogomi, Y.; Bessho, T.; Kinoshita, T.; Chantana, J.; Yoshino, K.; Shen, Q.; Toyoda, T.; Minemoto, T.; Murakami, T. N.; Segawa, H.; Hayase, S. Highly Efficient 17.6% Tin-Lead Mixed Perovskite Solar Cells Realized through Spike Structure. *Nano Lett.* **2018**, *18*, 3600-3607. DOI 10.1021/acs.nanolett.8b00701.

[28] Yao, K.; Wang, X.; Xu, Y.; Li, F.; Zhou, L. Multilayered Perovskite Materials Based on Polymeric-Ammonium Cations for Stable Large-Area Solar Cell. *Chem. Mater.* **2016**, *28*, 3131-3128. DOI 10.1021/acs.chemmater.6b00711.

[29] Wu, T.; Wang, Y.; Li, X.; Wu, Y.; Meng, X.; Cui, D.; Yang, X.; Han, L. Efficient Defect Passivation for Perovskite Solar Cells by Controlling the Electron Density Distribution of Donor-π-Acceptor Molecules. *Adv. Energy Mater.* **2019**, *9*, No. 1803766. DOI 10.1002/aenm.201803766.

[30] Arivunithi, V. M.; Reddy, S. S.; Sree, V. G.; Park, H.-Y.; Park, J.; Kang, Y.-C.; Shin, E.-S.; Noh, Y.-Y.; Song, M.; Jin, S.-H. Efficiency Exceeding 20% in Perovskite Solar Cells with Side-Chain Liquid Crystalline Polymer-Doped Perovskite Absorbers. *Adv. Energy Mater.* **2018**, *8*, No. 1801637. DOI 10.1002/aenm.201801637.

[31] Tao, C.; Neutzner, S.; Colella, L.; Marras, S.; Kandada, A. R. S.; Gandini, M.; De Bastiani, M.; Pace, G.; Manna, L.; Caironi, M. 17.6% Stabilized Efficiency in Low-Temperature Processed Planar Perovskite Solar Cells. *Energy Environ. Sci.* **2015**, *8*, 2365-2370. DOI 10.1039/C5EE01720C.

[32] Wu, Y.; Yang, X.; Chen, W.; Yue, Y.; Cai, M.; Xie, F.; Bi, E.; Islam, A.; Han, L. Perovskite Solar Cells with 18.21% Efficiency and Area over 1 cm^2 Fabricated by Heterojunction Engineering. *Nat. Energy* **2016**, *1*, No. 16148. DOI 10.1038/nenergy.2016.148.

[33] Yin, X.; Chen, P.; Que, M.; Xing, Y.; Que, W.; Niu, C.; Shao, J. Highly Efficient Flexible Perovskite Solar Cells Using Solution-Derived NiO_x Hole Contacts. *ACS Nano* **2016**, *10*, 3630-3636. DOI 10.1021/acsnano.5b08135.

[34] Jung, S.-K.; Heo, J. H.; Lee, D. W.; Lee, S.-C.; Lee, S.-H.; Yoon, W.; Yun, H.; Im, S. H.; Kim, J. H.; Kwon, O.-P. Nonfullerene Electron Transporting Material Based on Naphthalene Diimide Small Molecule for Highly Stable Perovskite Solar Cells with Efficiency Exceeding 20%. *Adv. Funct. Mater.* **2018**, No.1800346. DOI 10.1002/adfm.201800346.

[35] Shaikh, D. B.; Said, A. A.; Wang, Z.; Rao, P. S.; Bhosale, R. S.; Mak, A. M.; Zhao, K.; Zhou, Y.; Liu, W.; Gao, W.; Xie, J.; Bhosale, S. V.; Bhosale, S. V.; Zhang, Q. Influences of Structural Modification of Naphthalenediimides with Benzothiazole on Organic Field-Effect Transistor and Non-Fullerene Perovskite Solar Cell Characteristics. *ACS Appl. Mater. Interfaces* **2019**, *11*, 44487-44500. DOI 10.1021/acsami.9b13894.

[36] Jung, S.-K.; Heo, J. H.; Lee, D. W.; Lee, S.-H.; Lee, S.-C.; Yoon, W.; Yun, H.; Kim, D.; Kim, J. H.; Im, S.-H.; Kwon, O.-P. Homochiral Asymmetric-shaped Electron Transporting Materials for Efficient Non-Fullerene Perovskite Solar Cells. *ChemSusChem* **2019**, *12*, 224-230. DOI 10.1002/cssc.201802234.

[37] Liu, W.; Shaikh, D. B.; Rao, P. S.; Bhosale, R. S.; Said, A. A.; Mak, A. M.; Wang, Z.; Zhao, M.; Gao, W.; Chen, B.; Lam, Y. M.; Fan, W.; Bhosale, S. V.; Bhosale, S. V.; Zhang, Q. Molecular Aggregation of Naphthalene Diimide (NDI) Derivatives in Electron Transport Layers of Inverted Perovskite Solar Cells and Their Influence on the Device Performance. *Chem. Asian J.* **2020**, *15*, 112-121. DOI 10.1002/asia.201901452.

[38] Kim, H. I.; Kim, M. J.; Choi, K.; Lim, C.; Kim, Y.-H.; Kwon, S.-K.; Park, T. Improving the Performance and Stability of Inverted Planar Flexible Perovskite Solar Cells Employing a Novel NDI-Based Polymer as the Electron Transport Layer. *Adv. Energy Mater.* **2018**, *8*, No.1702872. DOI 10.1002/aenm.201702872.

[39] Wang, H.; Wu, J.; Zhang, Y.; Song, J.; Chen, L.; Xiao, Y.; Qu, J.; Wong, W.-Y. Achieving Efficient Green-Solvent-Processed Organic Solar Cells by Employing Ortho-Ortho Perylene Diimide Dimer. *Org. Electron.* **2020**, *83*, No. 105732. DOI 10.1016/j.orgel.2020.105732.

[40] Wang, H.; Chen, L.; Xiao, Y. Oxygen-Ether-Bridged Perylene Diimide Dimers: Efficient Synthesis, Properties, and Photovoltaic Performance. *Dyes Pigm.* **2020**, *180*, No. 108508. DOI 10.1016/j.dyepig.2020.108508.

[41] Wang, H.; Chen, L.; Xiao, Y. Constructing a Donor-Acceptor Linear Conjugation Structure for Heterologous Perylene Diimides to Greatly Improve the Photovoltaic Performance. *J. Mater. Chem. C* **2019**, *7*, 835-842. DOI 10.1039/c8tc04929g.

[42] Wang, H.; Fan, Q.; Chen, L.; Xiao, Y. Amino-Acid Ester Derived Perylene Diimides Electron Acceptor Materials: An Efficient Strategy for Green-Solvent-Processed Organic Solar Cells. *Dyes Pigm.* **2019**, *164*, 384-389. DOI 10.1016/j.dyepig.2019.01.047.

[43] Yang, F.; Zhang, P.; Kamarudin, M. A.; Kapil, G.; Ma, T.; Hayase, S. Addition Effect of Pyreneammonium Iodide to Methylammonium Lead Halide Perovskite-2D/3D Heterostructured

Perovskite with Enhanced Stability. *Adv. Funct. Mater.* **2018**, No. 1804856. DOI 10.1002/adfm.201804856.

[44] Gong, X.; Sun, Q.; Liu, S.; Liao, P.; Shen, Y.; Grätzel, C.; Zakeeruddin, S. M.; Grätzel, M.; Wang, M. Highly Efficient Perovskite Solar Cells with Gradient Bilayer Electron Transport Materials. *Nano Lett.* **2018**, *18*, 3969-3977. DOI 10.1021/acs.nanolett.8b01440.

[45] Ren, C.; He, Y.; Li, S.; Sun, Q.; Liu, Y.; Wu, Y.; Cui, Y.; Li, Z.; Wang, H.; Hao, Y.; Wu, Y. Double Electron Transport Layers for Efficient and Stable Organic-Inorganic Hybrid Perovskite Solar Cells. *Org. Electron.* **2019**, *70*, 292-299. DOI 10.1016/j.orgel.2019.03.033.

[46] Persson, I.; Lyczko, K.; Lundberg, D.; Eriksson, L.; Placzek, A. Coordination Chemistry Study of Hydrated and Solvated Lead (II) Ions in Solution and Solid State. *Inorg. Chem.* **2011**, *50*, 1058-1072. DOI 10.1021/ic1017714.

[47] Yang, F.; Hirotani, D.; Kapil, G.; Kamarudin, M. A.; Ng, C. H.; Zhang, Y.; Shen, Q.; Hayase, S. All-Inorganic $CsPb_{1-x}Ge_xI_2Br$ Perovskite with Enhanced Phase Stability and Photovoltaic Performance. *Angew. Chem. Int. Ed.* **2018**, *57*, 12745-12749. DOI 10.1002/anie.201807270.

[48] Yang, F.; Kamarudin, M. A.; Hirotani, D.; Zhang, P.; Kapil, G.; Ng, C. H.; Ma, T.; Hayase, S. Melamine Hydroiodide Functionalized $MAPbI_3$ Perovskite with Enhanced Photovoltaic Performance and Stability In Ambient Atmosphere. *Sol. RRL* **2019**, *3*, No. 1800275. DOI 10.1002/solr.201800275.

For Table of Contents Use Only